Chapter 3

Methodology

3.1 Software used

To generate the predicted stellar flux, the ATLAS9 model stellar atmosphere code (Kurucz, 1993) was used to produce monochromatic fluxes for a series of wavelengths ranging from 9 nm to 160,000 nm, with a resolution of 2 nm or less in the UV. Table 1 of Castelli & Kurucz (2004) contains precise details of the coverage in ($T_{\rm eff}$, $\log(g)$) parameter space, while a brief summary of the limits of the space is listed in Table 3.1. Four input metallicities were used for ATLAS9, at values of [Fe/H] = -2, -1, 0 and 0.5, covering the metallicities of most observed globular and open clusters.

The tables of bolometric corrections were generated using a FORTRAN 77 code incorporating the steps described in Section 2.3, inputs with tables describing the response functions of all three filter systems at the same wavelengths as those listed in the ATLAS9 model atmosphere tables, with the number of tables for each stellar metallicity value equal to the total number of ($T_{\rm eff}$, $\log(g)$) combinations available.

Once the bolometric correction tables were produced, all subsequent processes were written in Python 2.7 in the form of IPython notebooks. The repository containing all data, plots and programme codes for this project can be found at `https://github.com/AlexlwAstro/phd_work`.

The isochrones used were generated using the latest Bag of Stellar Tricks and

Parameter / unit	Minimum	Maximum	Number of values
$T_{\rm eff}$ / K	3500	50000	76
$\log(\ g\ /\ \mathrm{cm\ s^{-2}})$	0.0	5.0	11
[Fe/H]	-2.0	0.5	4

Table 3.1: Ranges for the input parameters for ATLAS9 atmospheric models

Isochrones (BaSTI) web interface (Pietrinferni et al. (2004), Hidalgo et al. (2018)). The filter systems whose throughput data were employed by BaSTI to generate the fluxes for the isochrones were ACS, WFC3 and Gaia-DR2. It should be noted that the WFC3 isochrone output does not include flux magnitudes for the F300X filter.

3.2 Extinction data

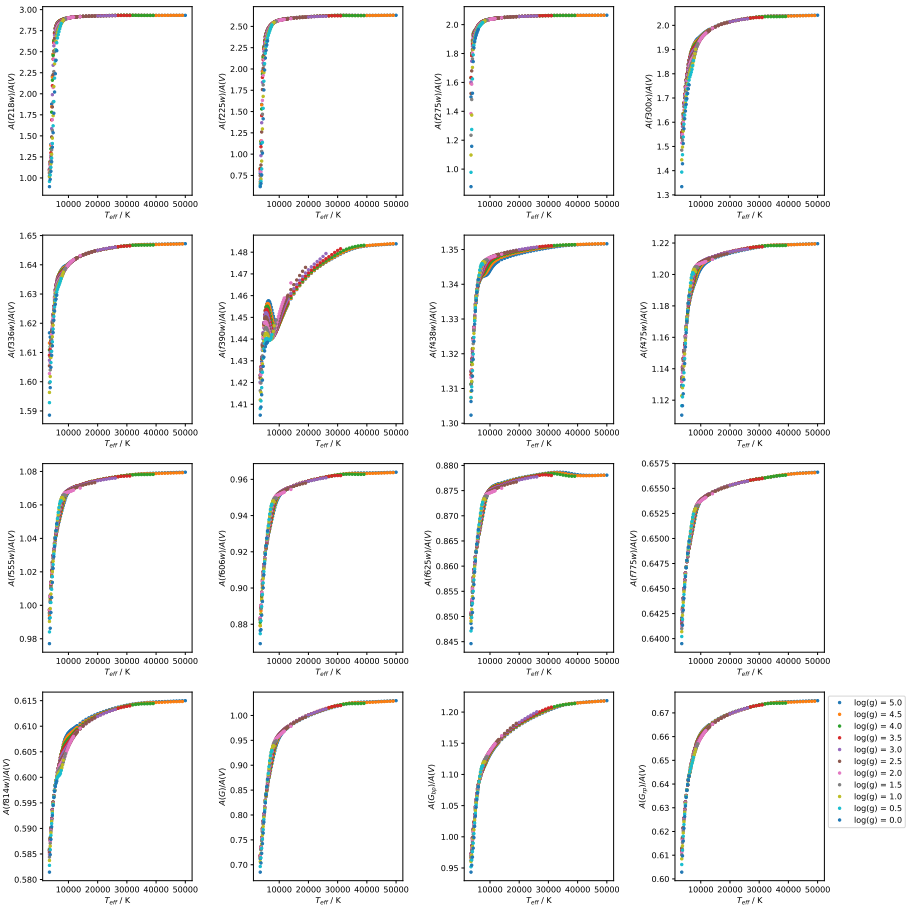

Figure 3.1: WFC3 and Gaia filter A_X/A_V data for [Fe/H] = -2, plotted against effective temperature, with each colour of dots representing a different value of $\log(g)$.

When calculating the bolometric corrections, the reference values taken by the parameters for Vega were:

1. $m_X^0 = 0.03$ for the Gaia filters
2. $m_X^0 = 0.00$ for the Hubble WFC3 filters

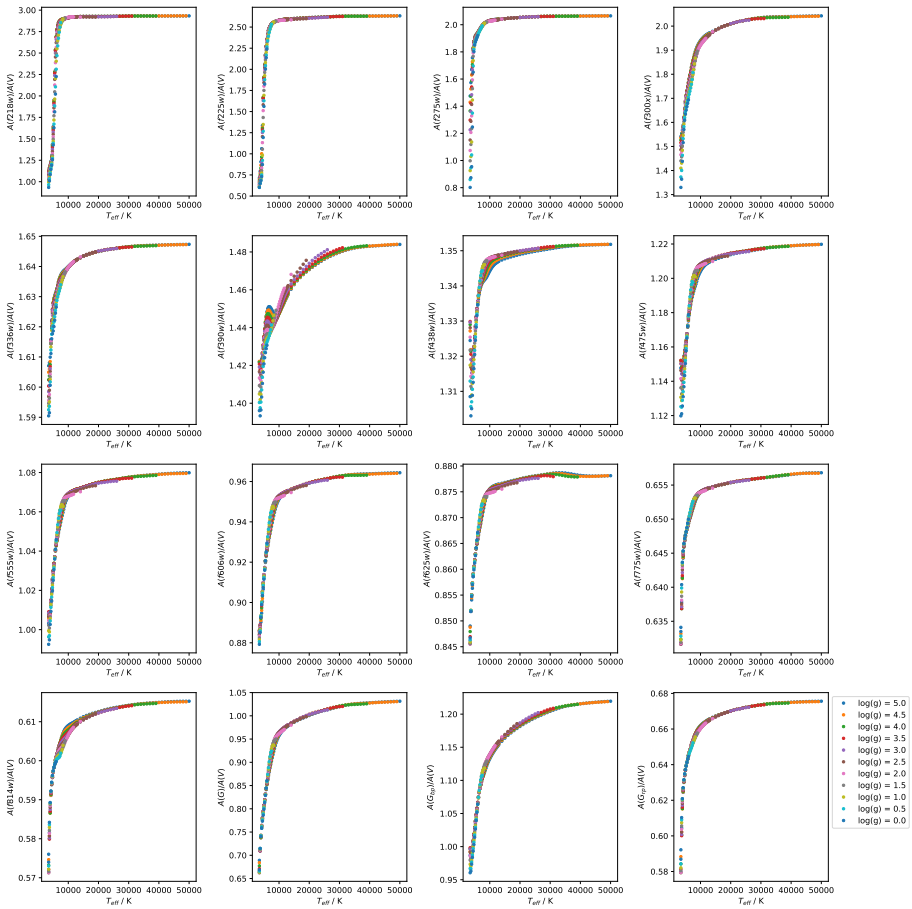

Figure 3.2: WFC3 and Gaia filter A_X/A_V data for [Fe/H] = 0.5, plotted against effective temperature, with each colour of dots representing a different value of $\log(g)$, showing the prominent presence of the tail-flick phenomenon in some filters.

together with $M_{\mathrm{bol},\odot} = 4.75$. The Vega model used in this project assumed $T_{\mathrm{eff}} = 9550\mathrm{K}$ and $\log(g) = 3.95$. The mean extinction law from Cardelli et al. (1989), as shown in Equation 1.6, with its different wavelength regimes for $a(x)$ and $b(x)$, was used with the A_V calibration values to simulate the extinction parameter in Equation 2.17. R_V was set to a value of 3.1, the standard value for the diffuse interstellar medium. The integration was carried out by iteratively adding the integrand results at regular small wavelength intervals. The non-zero calibration value of $A_V = 1$ was chosen, as this allows for significant changes in A_X/A_V from Equation (2.19), while also being close enough to zero to avoid significant changes in A_X/A_V due to the Forbes effect (Girardi et al., 2008).

To generate extinction-coefficient ratios A_X/A_V from the bolometric correction data, Equation 2.19 was used to calculate the differences between the $\mathrm{BC}(A_V = 0)$

and BC($A_V = 1$) datasets and thereby give a single dataset of mean A_X/A_V values (Girardi et al. (2008),Casagrande & VandenBerg (2014)).

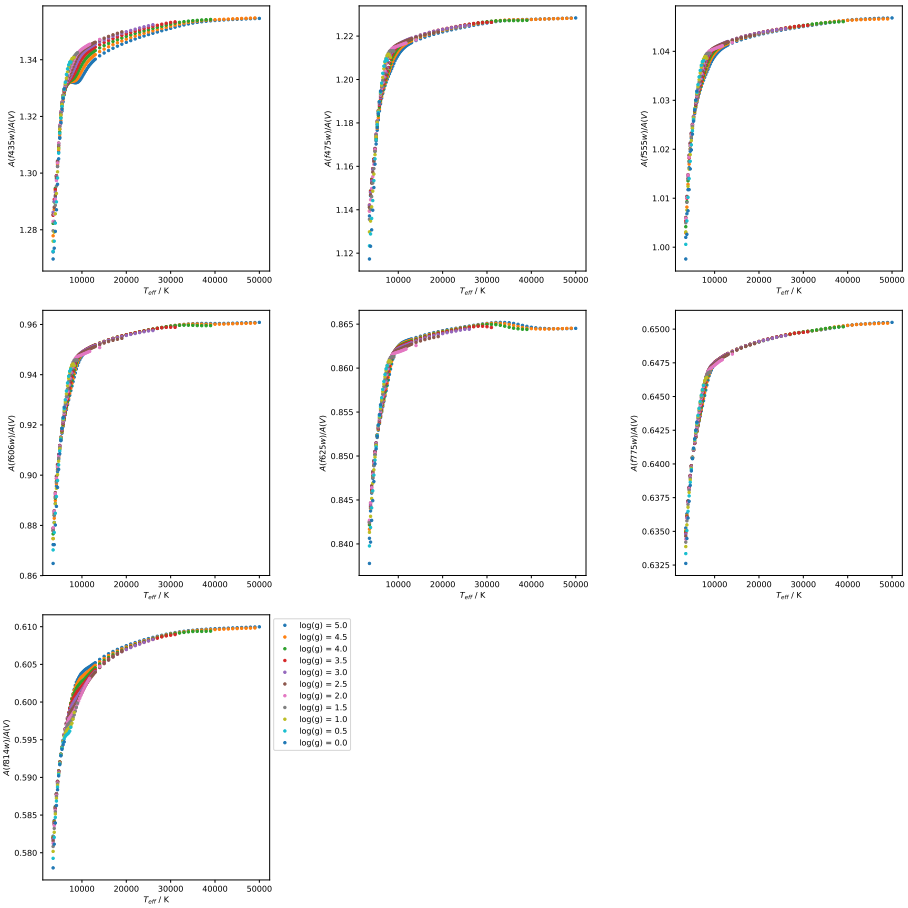

Figure 3.3: ACS filter A_X/A_V data for [Fe/H] = -2, plotted against effective temperature, with each colour of dots representing a different value of $\log(g)$.

As can be seen in the data displayed in Figures 3.1-3.4, in almost all of the filters studied in this project, the longer the central wavelength of a given filter throughput, the smaller the average value of A_X/A_V, independent of all other parameters. This conforms with the expectation resulting from the fact that the physical mechanisms causing extinction in the ISM preferential affect photons with shorter wavelengths.

Above $T_{\rm eff} \approx$ 12000-15000 K, the values of A_X/A_V are approaching a constant value as a function of all three input parameters. This is reflected in the choice of decay functions as the fitting functions for the data. This region of parameter space will be referred to henceforth as the "high-$T_{\rm eff}$ extinction plateau region" or simply "plateau".

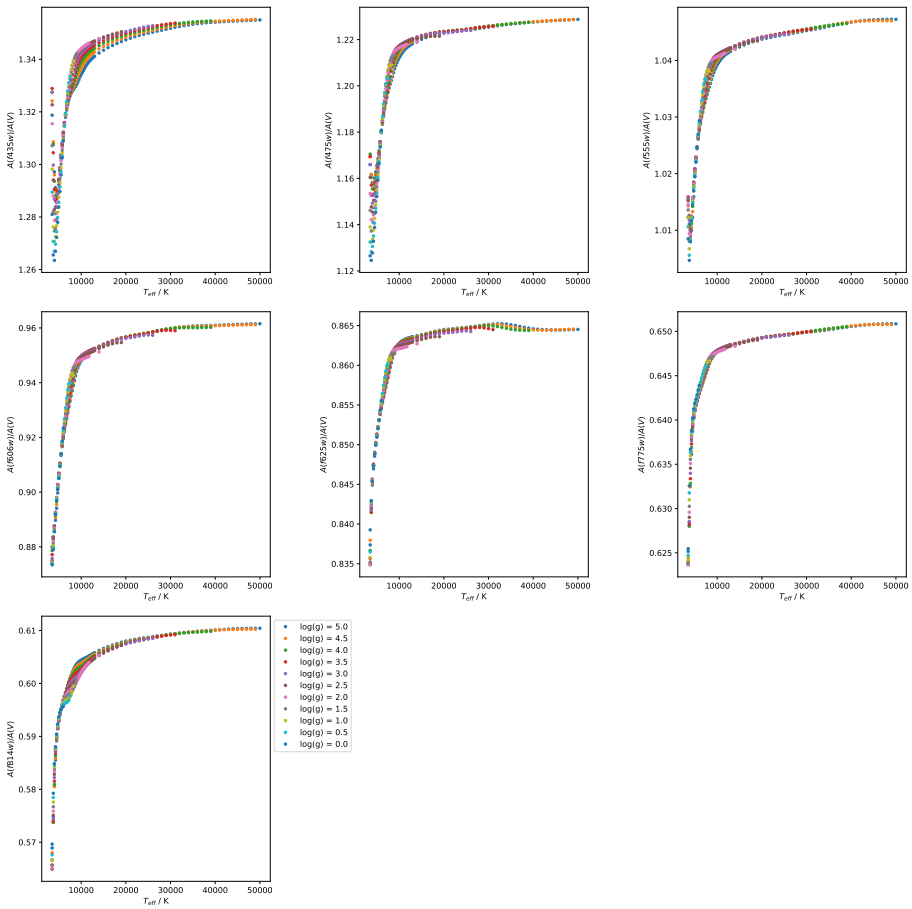

Figure 3.4: ACS filter A_X/A_V data for [Fe/H] = 0.5, plotted against effective temperature, with each colour of dots representing a different value of $\log(g)$, showing the prominent presence of the tail-flick phenomenon in some filters.

3.3 Finding & fitting functions

A property found in the data for some filters, more pronounced at higher metallicity but with a possible slight dependence on surface gravity, is the tendency of the gradient of A_X/A_V with increasing T_{eff} to become significantly less positive at the lowest temperatures in the data, typically 4000K and below. The spread in A_X/A_V values for different $\log(g)$ is typically about 0.2-04, with a linear progression from $\log(g) = 5.0$ at the lowest end to $\log(g) = 0.0$ at the highest. In some filters, at the highest metallicity employed ([Fe/H] = 0.5), this phenomenon causes the gradient to invert and become significantly negative, reversing the trend everywhere else in the data, including for the same filters at lower metallicity. Due to the shape of the resulting point-to-point line in these axes, it has been dubbed the "tail-flick" phenomenon. This was ignored as an artefact from the numerical integration required for Equation 2.17. This was due to the physical infeasibility of a cooler star experiencing a higher extinction A_X for a

globally-constant A_V value and metallicity, as was assumed for data in each BC table. In the relevant filters, only effective temperatures above those affected by the gradient inversion was used for fitting.

In order to find usable functions without running into issues with degeneracy between coefficients, the three input stellar parameters prioritising which parameters to model first, before expanding the function to include parts modelling the impact of other parameters and their associated coefficients. Too many coefficients created errors that were significantly greater in degenerate coefficients than in non-degenerate ones. This would obscure any useful information about the validity of the function form.

The bolometric flux of a black body can be calculated as the total area under the curve described by the Planck function per unit wavelength/frequency as a function of wavelength/frequency. Since stellar emission spectra can be reasonably approximated by a black body emission with absorption lines, it can be seen from Equation2.1 that the greatest effect on stellar spectra, and therefore on the extinction coefficient, will come from effective temperature. Therefore, the initial functions to be fitted were simple analytical functions of T_{eff} only:

$$A_{\text{pow}}(T_{\text{eff}}) = a(T_4)^b + c \tag{3.1}$$

$$A_{\text{exp}}(T_{\text{eff}}) = a\exp(bT_4) + c \tag{3.2}$$

where $T_4 = 10^{-4} \times T_{\text{eff}}$. The fitting operation was carried out on the data for solar metallicity ([Fe/H] = 0.0) and, because it gave the greatest number of T_{eff} data points, $\log(g) = 5$. This dataset will be referred to as the basic fitting data (BFD).

For the data in the Gaia filters, the opportunity was taken to compare the model for R_X and coefficients detailed for these filters by Casagrande & VandenBerg (2018). To apply their model to the extinction ratios used for this project, the definition of R_X was used to construct the following equation:

$$\frac{A_X}{A_V} = \frac{R_X}{R_V} = \frac{R_X}{3.1} \tag{3.3}$$

There were filters whose BFD could not support an accurate fit or maintain the desired accuracy across all combinations of $\log(g)$ and [Fe/H] using A_{pow} or A_{exp}. For these filters, more intricate functions were sought, including functions with explicit dependences on g and [Fe/H]. Several unsuccessful approaches were made before an acceptable function was found for each filter.

The most successful approach was plotting all the available data for each filter, in multiple 2D and 3D axes, and analysing it visually. The trends seen in the data were transcribed to find not only an overarching function template, akin to the status of A_{pow} and A_{exp}, but also smaller mathematical constructs within the template, such

as describing a decay coefficient in terms of $\log(g)$ and [Fe/H]. The details of the final form of the template as a function of each stellar parameter were deduced by fitting a logistic function of T_{eff} to the A_X/A_V data for each ([Fe/H],$\log(g)$) combination. This was decided on the basis that A_{exp} had been superior to A_{pow} in describing the data for all relevant filters and because, for these filters, the low-T_{eff} change in gradient appeared to be more significant than for others and the gradient was not inverted, as can be seen in Figures 3.2-3.3. This is still the case, even after accounting for the difference in A_X/A_V scale between filters. In particular, the T_{eff} gradient prior to the plateau appears to lead to an asymptote at lower, but still physically-viable, temperatures. This issue is resolved by the logistic function's property of converging to a constant value for both very high and low values of the input variable.

For a general logistic function in T_{eff}, there are four principle parameters:

- The global maximum value, denoted in this case by A_{max};
- The global minimum value, A_{min};
- The exponential decay coefficient, k;
- The T_{eff}-coordinate of the sigmoid midpoint, in this case T_0.

It was confirmed that this new function could describe each scenario accurately enough for further analysis. The resulting coefficients were tabulated and analysed for trends and, if found, the nature of those trends. This allowed for the incremental construction of sub-functions of $\log(g)$ and [Fe/H], making the overall function, A_{logis}, sensitive to all three input stellar atmosphere parameters, with effective temperature having the greatest effect and the relative effects of the other parameters dependent on the best-fit values of the relevant coefficients.

The sub-functions of $\log(g)$ and [Fe/H], upon inspection of the coefficients for the T_{eff}-only logistic function, were found to be simple functions of $\log(g)$ and [Fe/H], independent of T_{eff} variations. This allowed for them to be used as the definitions of T_0 and k, as shown in Equations 3.4 and 3.5, respectively.

$$T_0 = a\log(g) + b\left(\frac{[\text{Fe/H}]}{|[\text{Fe/H}]|^{1/2}}\right) + c \tag{3.4}$$

$$k = d\log(g) + e[\text{Fe/H}] + f \tag{3.5}$$

$$A_{logis}(T_{\text{eff}}, g, [\text{Fe/H}]) = \frac{(A_{max} - A_{min})}{(1 + \exp\left(-10^{-4}k(T_{\text{eff}} - T_0)\right))} + A_{min} \tag{3.6}$$

The final form was then subjected to a final fit on the entire A_X/A_V dataset, covering the entire (T_{eff}, $\log(g)$, [Fe/H]) parameter space available. A_{logis} was able to accurately reproduce the behaviour of almost the entire dataset. The details are given in Section 4.1.

Isochrone (Age/Myr , [Fe/H])	T_{eff} minimum	T_{eff} maximum	$\log(g)$ minimum	$\log(g)$ maximum
500,0.002	2870	9640	0.886	5.137
1000,0.002	2824	8035	1.608	5.184
5000,-1.049	3118	7112	0.456	5.318
10000,-1.049	3086	6412	0.286	5.332

Table 3.2: Ranges of effective temperature and surface gravities in selected BaSTI isochrones

3.4 Isochrone data fitting

To obtain isochrones from the BaSTI online database, the desired age range, initial metallicity and filter system must be specified. Therefore, the values of these quantities are shared by all stellar objects. For the stages in stellar evolution prior to the main-sequence turn-off, any changes in atmospheric metallicity are insignificant, due to the factors discussed in Section 1.3.

The output from the BaSTI database for each model stellar object gives the model's initial mass and current mass (i.e. after a time equal to the isochrone age), together with the logarithms of the stellar luminosity in solar units ($\log(L/L_{\odot})$) and of the effective temperature in K ($\log(T_{\text{eff}})$), followed by the absolute magnitudes (with zero extinction) of the object in each filter of the system. To derive the surface gravity g, we must combine Equation 2.1, to derive the stellar radius, and Equation 2.3. Equation 3.7 shows the resultant definition of g:

$$g = \frac{4\pi G M_{*} \sigma_{\text{SB}} T_{\text{eff}}^{4}}{L_{*}} \tag{3.7}$$

After this had been completed, each object had a co-ordinate in (T_{eff}, $\log(g)$) parameter space, plus the metallicity of the overall isochrone model. The filter magnitudes in the photometric data are the apparent magnitudes of the stars assigned to NGC 6793. Therefore, to match the quantities of the observational and isochrone datasets being compared, it was necessary to correct the observational data for distance and add extinction to the isochrones. This is that standard procedure used when analysing observational data. Thus, we were comparing the $M_{\text{ext},X}$ values for the isochrones and the observational data. The functions described in Section 3.3 were then applied to the dataset of stellar objects, producing values of $M_{\text{ext},X}$ for each filter for all objects, as is the standard for analysing observational data with unknown extinction coefficients.

The errors in the parallax data for objects assigned to NGC 6793 were significant, particularly for stars in the lower main-sequence - understandably, since they are the faintest objects in the data and therefore are more difficult to track against the background light sources. This leads to errors in the predicted $M_{\text{ext},X}$ magnitudes, which is calculated by rearranging Equation 2.7. The significance of the parallax errors in the

main sequence is such that, any differences between isochrones with similar parameters are rendered insignificant. This is the case irrespective of photometric errors in the observed fluxes from the photometric filters.

Since the table for photometric fluxes did not include photometric errors, the parallax errors alone accounted for the total error in the calculated $M_{\mathrm{ext},X}$. Therefore, the errors on the flux measurements were exactly equal in all filters for a given star. The errors on the $(G_{\mathrm{bp}} - G_{\mathrm{rp}})$ color index were calculated as standard, by adding the individual filter errors in quadrature, giving the color errors which were a factor of $\sqrt{2}$ greater than those for the individual filter fluxes.

When comparing the two approaches to extinction, in order to test for any differences in projected isochrone age via the MSTO, a range of ages must be considered. A "primary" age was utilised as the true cluster isochrone age. This primary isochrone was subjected to both the function-based (FBEC) and standard extinction-coefficient approaches. Two isochrones with ages equidistant from the primary were subjected to the standard approach only. All four of the resulting $M_{\mathrm{ext},X}$ isochrones were plotted together in the four chosen CMD axes, together with the original (zero-extinction) isochrone for visual reference.

This procedure was employed for two values of A_X/A_V standard fixed extinction treatment. Both were extracted from the ATLAS9 data tables for a $\log(g)$ value of 5.0 to represent a main-sequence star, highly desirable when comparing MSTO positions. The ATLAS9 metallicity chosen for calculating these A_X/A_V values was that which best matched the metallicity of the isochrone to which the coefficient was applied. The ATLAS9 value will be denoted $[\mathrm{Fe/H}]_{CM}$. The first value was equal to $(A_X/A_V)_{plat} = (A_X/A_V)(T_{\mathrm{eff}} = 50,000\mathrm{K}, \log(g) = 5.0, [\mathrm{Fe/H}]_{CM})$, and the second was equal to $(A_X/A_V)_{MS} = (A_X/A_V)(T_{\mathrm{eff}} = 5,000\mathrm{K}, \log(g) = 5.0, [\mathrm{Fe/H}]_{CM})$. This was done to reflect the fact that, on one hand, the assumption of a constant extinction coefficient is valid in the plateau region and, on the other, given the position of the MSTO in terms of stellar model T_{eff} values, it would be more prudent to ensure that the upper main sequences resulting from both approaches to extinction coincide in the CMD, making it easier to see any disagreements in the turn-off ages. For each of these plots, A_V was fixed at a value of 1.0.

Given the large number of filters studied in this project, four commonly-used CMD axes were selected to test for any effects of a function-derived A_X. Two of these are specific to the WFC3 system, with one CMD each for ACS and Gaia.

Cluster property	K05	GC18
Distance modulus / mag	10.73	8.894
-> distance / pc	1400	601
log(age / yr)	8.64	8.78
-> Age / Myr	437	603
$E(B-V)$ / mag	0.17	0.272
$[Fe/H]$	?	?
Members	? (> 3 ACSS-2.5)	465 (271 with Gaia photometry)

Table 3.3: Observational parameters for NGC 6793, according to Kharchenko et al. (2005) (WEBDA archive page) and Gaia Collaboration et al. (2018)

3.5 Observational test case: NGC 6793

To test the effects of the difference in treatment of A_X/AV on observational data, both cases were employed to predict the isochrone parameters (age,[Fe/H] and A_V) of the open cluster NGC 6793.

NGC 6793 has little information available in the literature when compared to open clusters. Two observational studies have been published which give estimates for the properties of the cluster. Both sets of results are listed in Table 3.3.

The Gaia DR2 dataset for NGC 6793, containing the parallaxes and apparent magnitudes (in all three Gaia filters) for 338 objects identified as belonging to the cluster, was obtained. The number of objects is greater than the 271 photometric Gaia objects found by Gaia Collaboration et al. (2018). In addition to this, there were significant variations in the observed parallaxes of individual stars, far beyond the maximum cluster radii expected (Schilbach et al. (2006)). Some objects were even assigned negative parallax values, which are therefore mathematically impossible. Restrictions on the parallax measurements were implemented, by imposing a distance-based selection range centred at 600 pc, which was treated as the centre of the cluster, in line with the Gaia Collaboration et al. (2018) estimate in Table 3.3. The range was decreased until the remaining sample size was approximately equal to 271. When this was implemented, the final sample of observational data for NGC 6793 contained 274 objects. Some of these objects still had parallax distances further from the cluster centre than would be expected for any star cluster. The size of the final dataset balanced the need for maintaining sufficient data points, to achieve a valid comparison to the previous studies of NGC 6793, and eliminating anomalous data.

The isochrone fitting to the NGC 6793 was done by eye using a plot of the cluster's observed Gaia CMD, the position of each star corrected for its parallax distance. Using the values of $E(B-V)$ and age from Gaia Collaboration et al. (2018), a standard-case isochrone was derived, again assuming a diffuse ISM (i.e., $R_V = 3.1$). The standard treatment was employed twice, creating a different isochrone each time. A coeffi-

cient calculated from $(A_X/A_V)_{MS}$ was applied in one case and one calculated using $(A_X/A_V)_{plat}$ in the other. The fitting process was carried out in sequential stages:

1. First, the upper main sequence of the FBEC isochrone was fitted to that of the standard-case isochrone by varying the value of A_V used to calculate the final FBEC value for each stellar object.

2. Next, the age of the FBEC isochrone was varied to match the observed turn-off location in the NGC 6793 data as far as possible.

3. Finally, the FBEC isochrone metallicity was varied in an attempt match the observed lower main-sequence.

The isochrone with the resulting parameters were then plotted alongside two standard-case isochrones, The resulting curves were compared to each other for accuracy with respect to the observational data.